Available online at www.sciencedirect.com

ScienceDirect

Geochimica et Cosmochimica Acta 249 (2019) 160–172

Geochimica et Cosmochimica Acta

www.elsevier.com/locate/gca

Experimental determination of pyrite and molybdenite oxidation kinetics at nanomolar oxygen concentrations

Aleisha C. Johnson [a,*], Stephen J. Romaniello [a], Christopher T. Reinhard [b], Daniel D. Gregory [c,d], Emilio Garcia-Robledo [e,f], Niels Peter Revsbech [e], Donald E. Canfield [g], Timothy W. Lyons [c], Ariel D. Anbar [a,h]

[a] School of Earth and Space Exploration, Arizona State University, Tempe, AZ 85287, United States
[b] School of Earth and Atmospheric Sciences, Georgia Tech, Atlanta, GA 30332, United States
[c] Department of Earth Sciences, University of California, Riverside, CA 92521, United States
[d] Earth Science Centre, University of Toronto, Toronto, ON M5S 3B1, Canada
[e] Aarhus University Centre for Water Technology, Dept. of Bioscience, Aarhus University, Denmark
[f] Department of Biology, University of Cadiz, 11510 Cadiz, Spain
[g] Department of Biology and the Nordic Center for Earth Evolution, University of Southern Denmark, Odense M, Denmark
[h] School of Molecular Sciences, Arizona State University, Tempe, AZ 85287, United States

Received 15 April 2018; accepted in revised form 11 January 2019; Available online 23 January 2019

Abstract

Constraining the rate at which sulfide minerals undergo oxidative weathering at low atmospheric O_2 is crucial for understanding the evolution of the Archean and Proterozoic biosphere when O_2 was a trace atmospheric gas. However, recent studies attempting to constrain sulfide oxidation rates, atmospheric O_2 sinks, and trace metal delivery to seawater under Archean conditions are limited by the need to extrapolate from experimental pyrite oxidation kinetics determined at much higher O_2 levels. Extrapolation of those data sets to Archean levels of O_2 ($<10^{-5}$ present atmospheric level or PAL prior to 2.4 Ga) leads to more than an order of magnitude uncertainty in sulfide mineral oxidation rates, hampering efforts to quantify oxidative weathering under early Earth conditions.

To quantify sulfide oxidation kinetics at low pO_2, we conducted aqueous pyrite and molybdenite oxidation experiments at ~2–1200 nM dissolved O_2 and pH values 1.83, 5.08, and 8.58. Our experimental approach used LUMOS O_2 sensors to extend the pO_2 range explored by oxidation experiments down to 10^{-5} PAL pO_2, the limit of the sensors, which is up to three orders of magnitude lower than the pO_2 range explored in previous work.

From these experiments, we use 28 independent rate measurements to derive a new rate law for the oxidation of pyrite as a function of pO_2:

$$r_{pyrite} = 10^{-8.83(\pm 0.27)}[O_2]^{0.50(\pm 0.04)}[H^+]^{-0.25(\pm 0.02)},$$

Where r_{pyrite} is the rate of oxidation in mol/m^2 sec, and the activities of dissolved $[O_2]$ and $[H^+]$ are in (mol/L). Our results most closely match the previous rate law presented by Williamson and Rimstidt (1994), but indicate a stronger pH dependence than previous studies. We also present the first kinetic rate law for molybdenite oxidation at low O_2, based on 13 independent rate measurements:

$$r_{molybdenite} = 10^{-8.3(\pm 2.3)}[O_2]^{0.5(\pm 0.3)},$$

Where $r_{molybdenite}$ is the rate of oxidation in mol/m^2 sec, and the activity of dissolved $[O_2]$ is in (mol/L). We find molybdenite oxidation to be nearly as rapid as pyrite oxidation even at low concentrations of dissolved O_2 (equivalent to $<10^{-5}$ PAL pO_2), in contrast to previous work which argued for a threshold effect for molybdenite oxidation. Both pyrite and molyb-

* Corresponding author.
E-mail address: acjohn29@asu.edu (A.C. Johnson).

https://doi.org/10.1016/j.gca.2019.01.022

denite oxidation kinetics exhibit a constant half-order dependence on dissolved O_2 down to nanomolar levels of O_2. We show that this behavior is best explained by a reaction mechanism in which O_2 undergoes dissociative adsorption to the sulfide mineral surface. This mechanism helps to resolve major uncertainties regarding the reaction mechanism of O_2 with pyrite and molybdenite mineral surfaces and provides a strong theoretical basis for the robust extrapolation of present results to higher and lower O_2 concentrations.

Keywords: Archean; Oxidative Weathering; Pyrite, Molybdenite; Oxidation Kinetics

1. INTRODUCTION

Laboratory measurements of pyrite oxidation kinetics are used to estimate rates of oxidative weathering in a variety of modern and ancient environments (Bolton et al., 2006; Reinhard et al., 2009; Konhauser et al., 2011; Stüeken et al., 2012; Reinhard et al., 2013; Johnson et al., 2014; Daines et al., 2017). The models using these rate laws provide quantitative constraints on Earth's earliest sulfur and oxygen cycles, with important implications for the availability of O_2, sulfate, and trace metals for biological processes (Anbar et al., 2007; Scott et al., 2008; Reinhard et al., 2009; Stüeken et al., 2012; Gregory et al., 2017). Evidence in the rock record suggests that transient episodes of oxygenation ('whiffs of O_2') and subsequent sulfide oxidation on the continents were responsible for mobilizing redox-sensitive metals such as Mo and Re to seawater (Anbar et al., 2007; Kendall et al., 2015). These episodes of oxidative weathering were also responsible for expanding the lateral extent of ocean euxinia prior to the oxygenation of Earth's atmosphere through elevated delivery of sulfate to the oceans (Reinhard et al., 2009; Stüeken et al., 2012).

During oxidative weathering by O_2, pyrite reacts with O_2 in the presence of water to produce ferrous iron, sulfate, and acid:

$$FeS_2 + \frac{7}{2}O_2 + H_2O \rightarrow Fe^{2+} + 2SO_4^{2-} + 2H^+, \quad (low\ pH) \tag{1}$$

$$FeS_2 + \frac{15}{4}O_2 + \frac{7}{2}H_2O \rightarrow Fe(OH)_3 + 2SO_4^{2-} + 4H^+, \quad (neutral\ and\ high\ pH) \tag{2}$$

The rates of these reactions are determined by the concentrations of O_2 and pH. Several previous studies have compiled experimentally determined reaction rates to derive kinetic rate laws (Smith and Shumate, 1970; McKibben and Barnes, 1986; Nicholson et al., 1988; Moses and Herman, 1991; Ciminelli and Osseo-Asare, 1995; Gartman and Luther, 2014). The most widely used rate law is that compiled by Williamson & Rimstidt (1994):

$$r\left(molm^{-2}s^{-1}\right) = 10^{-8.19}[O_2]^{0.50}[H^+]^{-0.11} \tag{3}$$

where the activities of dissolved $[O_2]$ and $[H^+]$ are in (mol/L).

Modeling studies exploring the role of sulfide oxidation on early Earth have traditionally extrapolated these O_2-dependent rate laws to Archean pO_2 values ($<10^{-5}$ PAL, < 3 nM) (Canfield et al., 2000; Anbar et al., 2007; Reinhard et al., 2009; Reinhard et al., 2013; Johnson et al., 2014; Daines et al., 2017). However, this approach requires extrapolating oxidation kinetics to pO_2 values several orders of magnitude below the experimentally determined range (0.001–1 atm pO_2). Experiments have been limited to near-present and greater atmospheric pO_2 because of the difficulty associated with not only removing, but also precisely measuring, dissolved O_2 concentrations or the products of pyrite oxidation in the submicromolar range.

Due to these limitations, extrapolation of pyrite oxidation kinetics from different rate laws results in significant disagreement regarding pyrite oxidation rates at Archean pO_2 (Nicholson et al., 1988; Williamson and Rimstidt, 1994; Bolton et al., 2006). More broadly, without a better mechanistic understanding of sulfide oxidation kinetics at low O_2, it is not possible to discern which rate laws are more likely to be correct (Evangelou and Zhang, 1995; Rimstidt and Vaughan, 2003; Chandra and Gerson, 2010).

Most previous studies of sulfide oxidation focus on pyrite because it is the major sulfide mineral present in Earth's upper crust. However, due to our particular interest in the release of Mo to the oceans during oxidative weathering, we also examined the oxidation kinetics of molybdenite (MoS_2), which is the major carrier of Mo in igneous sulfides (Greaney et al., 2016). Molybdenite reacts with O_2 and water to form the soluble molybdate ion, sulfate, and acidity:

$$MoS_2 + \frac{9}{2}O_2 + 3H_2O \rightarrow MoO_4^{2-} + 2SO_4^{2-} + 6H^+ \tag{4}$$

There are relatively few studies of molybdenite oxidation under natural conditions, and none of these studies reports a kinetic rate law. Greber et al. (2015) provided an initial reconnaissance of molybdenite oxidation at nM concentrations of dissolved O_2. Although this study was able to detect molybdenite oxidation at low O_2, it did not attempt to provide a kinetic rate law or elucidate the reaction mechanism for molybdenite oxidation. As a result, molybdenite oxidation kinetics in the presence of Archean and Proterozoic levels of O_2 remain poorly understood, limiting our understanding of molybdenum delivery to the ancient oceans.

To generate relevant rate laws for pyrite and molybdenite oxidation as a function of pO_2 under low-O_2 conditions, we performed aqueous pyrite and molybdenite oxidation experiments at nanomolar O_2 concentrations using luminescence-measuring oxygen sensors (LUMOS, Lehner

et al., 2015). These sensors are sensitive to dissolved O_2 concentrations between 1–1200 nM O_2, allowing us to measure sulfide oxidation rates at O_2 levels much lower than those possible in previous studies. Our dataset extends the range of pO_2 explored in sulfide oxidation experiments to $\sim 10^{-5}$ PAL, allowing us to derive a new rate law and provide new insights regarding oxidation mechanism. Our experimental results open new opportunities for exploring the implications of sulfide weathering at varying levels of atmospheric O_2.

2. METHODS

We performed a total of nine mixed flow reactor experiments to measure pyrite and molybdenite oxidation rates as a function of O_2 and pH. Pyrite oxidation experiments were performed in duplicate under three different pH conditions (1.83, 5.03, and 8.58). Molybdenite was explored in the remaining three experiments at pH 1.83, 5.03, and 9.48.

Pyrite oxidation experiments were performed using trace metal-grade FeS_2 powder from Sigma Aldrich (<0.2% trace metals, ~325 mesh, PN Aldrich-778117) (Fig. S1) to ensure consistency and minimize effects from impurities. Pyrite powders were analyzed with XRD to confirm they were pyrite and not marcasite (Fig. S2). Initial experiments with molybdenite powder (<2 μm diameter) proved difficult, as its extreme hydrophobicity, especially as small grains, resulted in pervasive floating, clumping, and trapped air bubbles. To avoid these problems, we ultimately used large flakes of molybdenite, which were prepared by manually flaking cm-scale molybdenite grains purchased from Ward's Science (PN 470178-584). The large molybdenite flakes limited the surface area available for reaction but minimized wetting issues, which we viewed to be more important.

Prior to the experiments, the pyrite powder was repeatedly rinsed with methanol in an ultrasonic bath to remove fine particles following the method reported by McKibben (1984). Once the methanol rinses no longer contained visible fines, the powder was then rinsed in 2% nitric acid for 30 seconds to remove oxide coatings. After a final methanol rinse, the powder was left to dry in an anaerobic hood (<20 ppm O_2) to limit contact with O_2 and prevent unwanted oxidation.

For the molybdenite grains, no methanol rinse was needed to remove fines because the grains were flaked, so fines were easily avoided. Instead of rinsing with nitric acid, the outer layers were manually flaked off to remove potentially oxidized outer layers; only interior layers with fresh surfaces were used in the experiments. Samples were stored in an anaerobic hood to prevent oxidation. Any fines produced by flaking were lost during the filling of the reactors because small (<1 mm) grains floated out when the reactors overflowed. Several grams of both pyrite and molybdenite were prepared for each type of experiment. Splits of each mineral type were analyzed by N_2–BET to determine the initial specific surface area.

Experimental solutions were prepared at three different pH values. Titrants were chosen carefully to be analogous to the solutions of previous experimental studies, and when possible, to natural conditions. The pH 2 solution was prepared by diluting reagent grade sulfuric acid with 18.2 MΩ-cm DI water to a final concentration of 0.01 M. The pH 5 solution consisted of a 0.1 M acetate buffer prepared using acetic acid and sodium acetate. The pH 8 solution was prepared by dissolving sodium bicarbonate in 18.2 MΩ-cm DI water to a final concentration of 0.1 M. Solutions were autoclaved in loosely capped Pyrex bottles to exclude microbes and preclude the need for a sterilization agent in the experiments. Immediately prior to the experiments, the solutions were vigorously sparged with Ar for 30 min to remove dissolved O_2. We found Ar gas, supplied from a liquid Ar dewar, to be more effective than N_2 gas from a compressed gas cylinder in avoiding trace O_2 gas contamination. The pH of the final solutions was measured after sparging with Ar, since CO_2 loss was expected to increase the starting pH of the solutions, particularly for the bicarbonate solution. Final buffer pH values varied slightly from targeted values as anticipated (Tables 1 and 2).

Experiments were conducted in custom-made 1100 mL sealed glass reactors using luminescence-measuring O_2 sensors (LUMOS) to optically measure concentrations of dissolved O_2 to single digit nanomolar concentrations and thus to monitor reaction progress (Fig. 1) (Lehner et al., 2015; Garcia-Robledo et al., 2017). The optical sensor on the outside of the glass wall of the reactor pulses 405 nm light and monitors the fluorescence of an optode spot mounted on the inside of the reactor wall. O_2 in solution will quench this fluorescence, and the rate of the quenching reaction can be calibrated and used to calculate the concentration of dissolved O_2 (Lehner et al., 2015).

Prior to each experiment, bottles were rinsed with 0.1 M HCl, followed by 0.1 M NaOH. These rinses inhibit microbial growth. Sterilization by autoclaving was not performed because it would have destroyed the optode spots. Sterilization agents, such as mercuric chloride or formalin, were avoided as they may have formed complexes with the mineral surface. To test if our procedures were sufficient to prevent microbial growth and thus biological consumption of O_2, we conducted a control experiment for each pH condition in which we measured the dissolved O_2 concentrations of Ar-purged solutions within the reactors for two to three weeks. We observed no significant changes in O_2 concentrations over this time, confirming that there was no significant consumption of O_2 due to microbial growth and no significant contamination from the atmosphere once the reactors were sealed.

Mineral powders were removed from the anaerobic hood and placed into the reactor bottles along with glass-coated 60 × 8 mm magnetic stir bars (Cowie Technology). PTFE stir bars and all other plastic and polymer components must be strictly avoided since they slowly degas O_2, thereby contaminating low-level O_2 experiments. A continuous flow of N_2 was maintained while filling the bottles to limit the introduction of atmospheric O_2 to the solutions during filling. The Ar-purged solutions were siphoned into the bottles until they overflowed. Siphoning, rather than pouring, avoids any contact of the solutions with the atmosphere, which could entrain atmospheric O_2. Bottles were

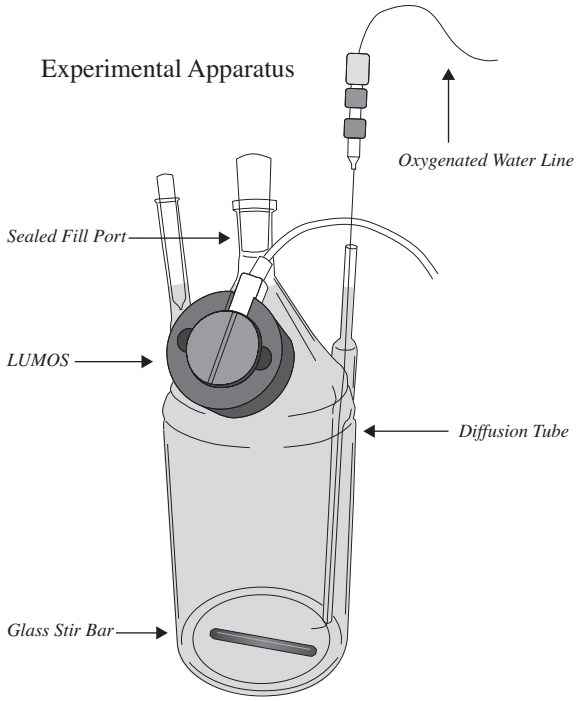

Fig. 1. Schematic of experimental apparatus and LUMOS sensor used in this study. Particles were kept suspended in solution with the glass stir bar.

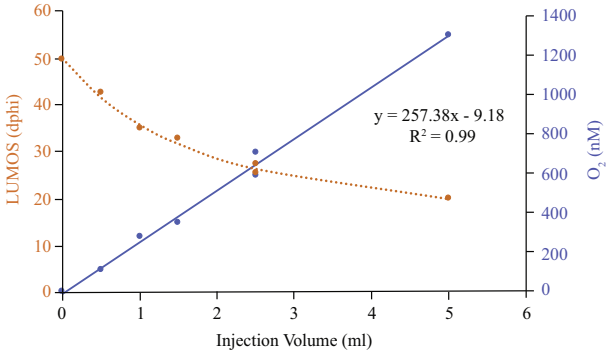

Fig. 2. Example of calibration data with 6 injections of oxygenated water. Orange data are read out from the sensor in dphi (change in phase shift) and blue data are calculated from the calibration curve for nM O_2 (Lehner et al., 2015). (For interpretation of the references to colour in this figure legend, the reader is referred to the web version of this article.)

sealed with ground glass stoppers. Putty (Hasbro Inc.) was wrapped around the outside of the stoppers to prevent the seals from drying out. Stirring rates were set to >100 rpm to keep particles suspended in solution and to limit mineral grinding.

In many studies of sulfide oxidation kinetics, oxidation rates are determined by monitoring production rates of iron and sulfate, along with decreases in pH. However, at the low concentrations of O_2 present in the experiments, reaction kinetics are so slow that this approach was not practical. Instead, reaction kinetics were determined by tracking the consumption of O_2 and by assuming congruent dissolution. This assumption is evaluated below in Section 4.1.1.

We used three reactors in parallel. During each set of experiments, we ran two duplicate pyrite experiments and one molybdenite experiment at a single pH. Each set of experiments lasted a total of two to five weeks. The LUMOS O_2 sensors were calibrated by allowing the O_2 concentration in the reactor to be drawn down by mineral oxidation to less than 1 nM O_2, after which precisely known volumes of oxygenated (air-equilibrated) deionized water were injected into the reactor using a syringe (Fig. 2).

Once the sensors on each reactor were calibrated, oxygenated water was slowly and continuously injected with a syringe pump (New Era NE-1600). Steady state was reached when O_2 consumption via mineral oxidation, together with a nearly negligible solution outflow (O_2-$_{Out}$), exactly equaled the rate of O_2 addition via the continuous injection of oxygenated water (O_2-$_{In}$). By increasing the flow rate of the syringe pump (O_2-$_{In}$), the O_2 supply suddenly exceeds consumption, causing the concentration of dissolved O_2 in the bottle to increase. This in turn increases the rate of mineral oxidation, which causes a new steady state to be reached at a higher pO_2 (mineral oxidation [O_2-$_{Out}$] matches O_2-$_{In}$). This technique allowed us to calculate the rate of oxidation for a sample of known surface area at different concentrations of dissolved O_2. Pyrite oxidation experiments containing 1.48–3.33 grams of pyrite powder were conducted with flow rates of 0.1–9.0 ml/h. Due to the lower surface area in the molybdenite experiments, flow rates between 0.01 and 0.6 ml/h were used for experiments containing 1.82–5.60 grams of molybdenite flakes.

Experiments were run for periods of several weeks each, with data recorded every 10–30 seconds. The syringe pump flow was typically set for a period of several days before a new flow rate was set. Steady states were determined by analyzing plateaus in the data (Fig. 3) for relative standard deviation (<10%) and slope (<6% slope change/h).

After each experiment, the glass reactors were moved to an anaerobic hood. Experimental solutions were filtered using a bottle-top vacuum filter system to recover the powders (Millipore Stericup 0.22 µm, catalogue number SCGPU05RE). Powders were allowed to dry inside the anaerobic hood and were then subsequently reanalyzed for surface area using N_2-BET. When there were only small changes in surface area, the post-experiment surface area was used for the rate calculations. When significant surface area changes were observed, the average of the pre- and post- surface areas was used for rate calculations, and error propagation was used to report the final rate uncertainty based on the total surface area change.

At steady state, the reactor O_2 budget yields:

$$r_{O_2} = -\frac{(m_{in} - m_{out})r_{flow}}{A} \quad (5)$$

$$r_{pyrite} = -\frac{2}{7}r_{O_2} \quad (6)$$

where r_{O2} and r_{pyrite} are in mol/m^2 sec, m_{in} and m_{out} are the dissolved O_2 concentrations of the incoming and outgoing solutions in mol/L, r_{flow} is the flow rate in L/sec, and A is

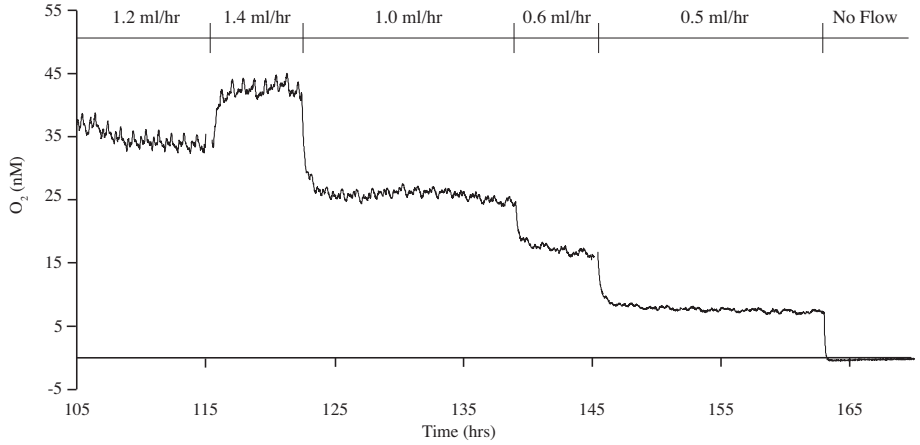

Fig. 3. Sample of raw dissolved O_2 concentration data from a pyrite oxidation experiment at pH 5 where flow was varied from 1.4 ml/h (382.2 nmol O_2/h) to 0.5 ml/h (136.5 nmol O_2/h) over the course of 65 hours.

the total surface area of the mineral powder in m^2. At each flow rate, the steady state O_2 concentration in each reactor was calculated by averaging the data points of the plateau of oxygen concentration, with relative standard deviation from the mean reported as the uncertainty (see Fig. 3 for examples of plateaus observed). The specific oxidation rate corresponding to each oxygen concentration plateau was calculated using the known O_2 fluxes, the known mass and specific surface area of mineral in each experiment, and the corresponding reaction stoichiometry. Raw data and rate calculations are presented in Tables S1 and S2.

3. RESULTS

Fig. 3 shows the O_2 concentration time series for a typical experiment (pyrite, pH = 5, bottle 3). Data for each experiment and accompanying rate data are summarized in Table 1, with supporting data provided in Table S1.

The calculated O_2 consumption rates for all pyrite oxidation experiments are plotted in Fig. 4 as a function of dissolved O_2 (log mol/L) and atmospheric pO_2 (in PAL), where pO_2 is calculated as the equilibrium partial pressure of O_2 for a given O_2 concentration in solution ($K_H = 770$ L atm/mol for O_2 in non-saline water at 25 °C, Sander, 2015). Our data extend pyrite oxidation rates as a function of pO_2 down to $\sim 10^{-5}$ PAL. The slope of each pH dataset indicates the order of reaction with respect to pO_2.

To determine the best-fit parameters in establishing a kinetic rate law, we performed a multivariate errors-in-variables regression of the pyrite oxidation dataset (using a Monte Carlo approach) yielding:

$$r_{pyrite} = 10^{-8.83(\pm 0.27)}[O_2]^{0.50(\pm 0.04)}[H^+]^{-0.25(\pm 0.02)}, \quad (7)$$

where r_{pyrite} is the oxidation rate in mol/m^2 sec, and the activities of dissolved $[O_2]$ and $[H^+]$ are in (mol/L). Data for molybdenite oxidation rates are summarized in Table 2 and Fig. 5, with supporting data presented in Table S2. As for pyrite, errors in the oxidation rates were calculated from uncertainties in the surface area measurement. Taking these uncertainties into account, variations in rate as a function of pH were not found to be statistically significant. A York regression of the dataset independent of pH results in the following rate law:

$$r_{molybdenite} = 10^{-8.3(\pm 2.3)}[O_2]^{0.5(\pm 0.3)}, \quad (8)$$

where $r_{molybdenite}$ is the oxidation rate in mol/m^2 sec, and the activity of dissolved $[O_2]$ is in (mol/L).

Table 1
Results from duplicate pyrite oxidation experiments at a range of pH's and dissolved O_2.

pH	$[O_2]$ (nM)	r_{pyrite} (mol/m^2 sec) × 10^{13}
8.58	14.6 ± 0.9	190 ± 80
	43 ± 3	300 ± 100
	81 ± 2	400 ± 200
	138 ± 2	600 ± 200
	42 ± 1	595 ± 680
	127 ± 3	1000 ± 1000
	282 ± 2	1000 ± 2000
5.08	35 ± 1	70 ± 50
	42.6 ± 0.9	90 ± 60
	25.7 ± 0.7	60 ± 40
	16.5 ± 0.4	40 ± 30
	7.5 ± 0.3	30 ± 20
	10.3 ± 0.4	24 ± 6
	13.5 ± 0.4	28 ± 8
	7.6 ± 0.3	20 ± 5
	5.1 ± 0.2	12 ± 3
	2.0 ± 0.1	10 ± 3
1.83	786 ± 3	40 ± 10
	275 ± 2	29 ± 8
	134 ± 2	19 ± 5
	34.7 ± 0.5	10 ± 3
	8.7 ± 0.4	5 ± 1
	1234 ± 4	40 ± 9
	923 ± 2	32 ± 7
	538 ± 2	24 ± 5
	286 ± 2	16 ± 3
	73.9 ± 0.8	8 ± 2
	16.7 ± 0.5	4 ± 1

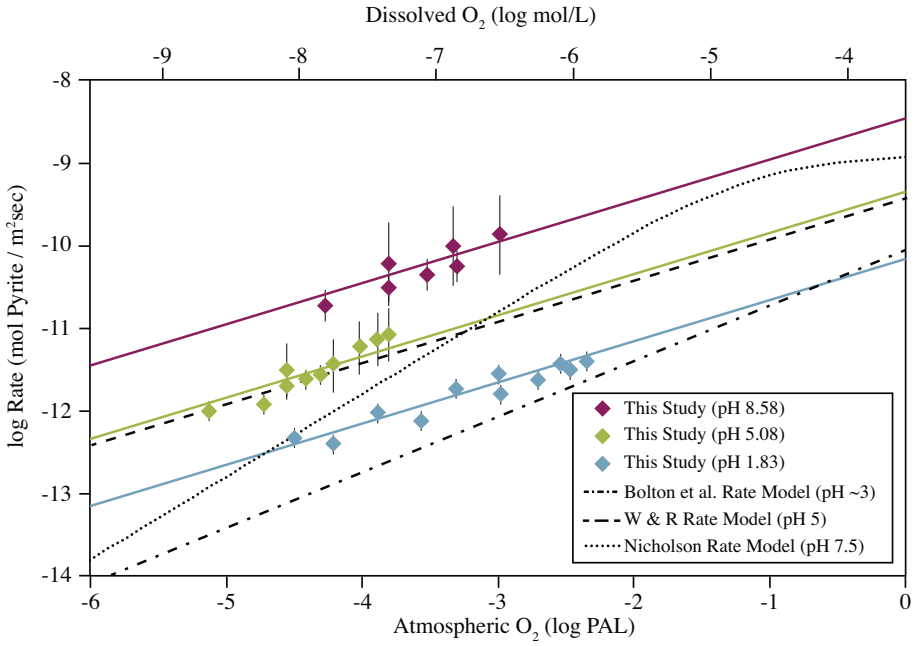

Fig. 4. Experimentally constrained rates of pyrite oxidation as a function of pO_2 and pH. Colors indicate rates collected at pH 1.83, 5.08, and 8.58. Solid lines are the rate law we present plotted at pH's corresponding to the experiments. Dashed lines are extrapolations of the rate law published by Williamson & Rimstidt (1994) at pH 5, Nicholson et al. (1988) at pH 7.5, and a rate law used by Bolton et al. (2006) based on the data of Smith and Shumate (1970) at approximately pH 3. Uncertainties were determined by propagating uncertainty in the surface area measurement.

Table 2
Results from molybdenite oxidation experiments at a range of pH's and dissolved O_2.

pH	$[O_2]$ (nM)	$r_{molybdenite}$ (mol/m^2 sec) × 10^{13}
9.48	643 ± 8	80 ± 40
	490 ± 3	40 ± 20
	4.4 ± 0.4	15 ± 8
	230 ± 3	40 ± 20
5.08	32 ± 2	6 ± 5
	2.8 ± 0.5	10 ± 10
	4.9 ± 0.8	20 ± 20
	43 ± 3	30 ± 30
	375 ± 3	70 ± 60
1.83	153 ± 1	30 ± 10
	41.8 ± 0.7	13 ± 6
	655 ± 3	40 ± 20
	291.4 ± 0.8	13 ± 6

4. DISCUSSION

Our oxidation experiments at low O_2 allow us to resolve discrepancies among prior pyrite oxidation rate laws, which can largely be accounted for by small differences in the order of reaction with respect to O_2 and differences in experimental pH (see below). In addition, we quantify for the first time the efficiency of molybdenite oxidation at low O_2 and develop a mechanistic interpretation of sulfide oxidation that supports a surface-mediated reaction. Finally, we discuss the implications of these data for global sulfide weathering models.

4.1. Pyrite Oxidation Rates

4.1.1. Rate vs. [O_2]

Our pyrite oxidation rates are generally in good agreement with the rates predicted by the rate law compilation of Williamson and Rimstidt (1994). The order of reaction with respect to O_2, 0.50 ± 0.04, indicated by our rate law is the same as the 0.50 order of reaction determined by Williamson and Rimstidt (1994) (Fig. 3). This half-order rate law is also consistent with many prior experimental studies (McKibben and Barnes, 1986; Williamson and Rimstidt, 1994; Ciminelli and Osseo-Asare, 1995; Liu et al., 2008a,b).

Furthermore, the pyrite oxidation rates we calculate using the rates of O_2 consumption and the reaction stoichiometry in Eq. (1) are consistent with previous experiments which determined pyrite oxidation kinetics by tracking the production of sulfate or dissolved Fe (McKibben and Barnes, 1986; Nicholson et al., 1988; Moses and Herman, 1991). This finding is important because it confirms that our approach of measuring O_2 consumption is stoichiometrically consistent with approaches that measure reaction products.

While our rate law agrees with that of Williamson and Rimstidt (1994), the rate law slopes inferred by Bolton et al. (2006) and Nicholson et al. (1988) are steeper (0.67 and 1.0, respectively), predicting very different oxidation rates at low O_2. In Bolton et al. (2006), the higher order dependency of pyrite oxidation rate on oxygen concentration resulted from a linear regression of the data from Smith and Shumate (1970), which suffers from the lack of data at lower O_2 concentrations. Nicholson et al. (1988)

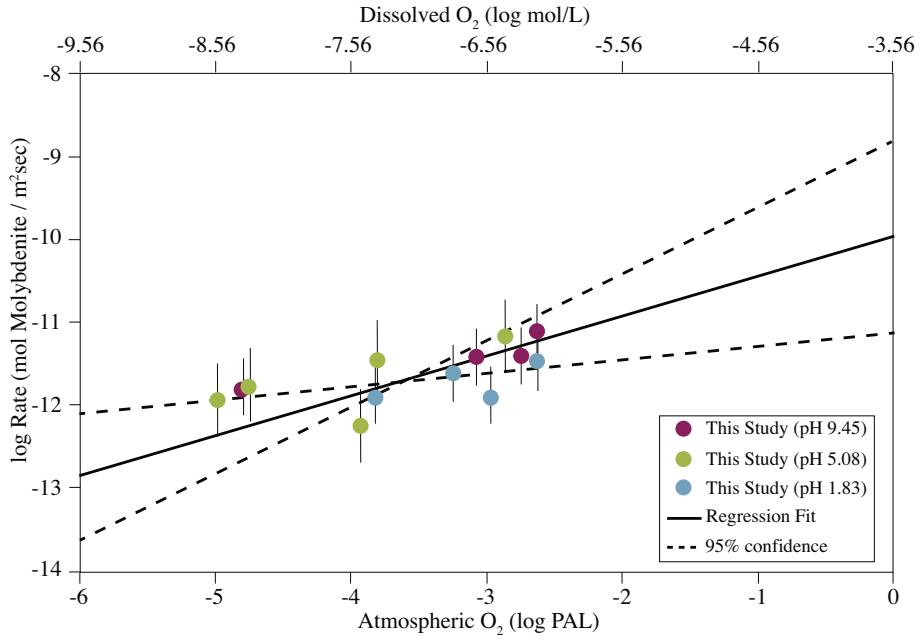

Fig. 5. Rate of molybdenite oxidation as a function of pO_2 and pH. Symbol color indicates pH of the experimental solution. Uncertainties were determined by propagating uncertainty in the molybdenite surface area measurement. Uncertainty in the regression fit is plotted here as dashed lines to depict the 95% confidence interval in the slope of the line.

proposed that pyrite oxidation rates were limited by adsorption of O_2 to the pyrite mineral surface. This mechanism leads to a saturation curve that should display first-order dependency of pyrite oxidation on oxygen concentration at nanomolar concentrations of O_2 and fractional-order dependency at higher O_2. Our data are not consistent with this saturation curve model and instead suggest that the order of reaction with respect to O_2 is half-order at all levels of O_2. We discuss the implications of this observation for oxidation mechanisms in Section 4.3.

4.1.2. Rate vs. $[H^+]$

Our pyrite oxidation kinetics show a pH dependence that is stronger than reported in previous studies. While our oxidation rates at pH 5.08 match very well with the previous literature (the compilation of Williamson and Rimstidt (1994) in particular), our high pH experiments yield pyrite oxidation rates that are slightly faster than predicted by previous work. Likewise, in the low pH range, our oxidation rates are slower than expected. Our regression indicates an order of reaction with respect to $[H^+]$ of -0.25 ± 0.02. Experimental values of pH dependency cited in the literature vary widely from −0.43–0.14, but most converge on −0.1 (Smith and Shumate, 1970; Williamson and Rimstidt, 1994; Ciminelli and Osseo-Asare, 1995; Paschka, 2001; Liu et al., 2008a).

One possible explanation for the stronger pH dependence we observed could be the differences in experimental design. In previous studies, oxidation rates in low-pH experiments may have been accelerated by the presence of dissolved ferric iron produced from pyrite oxidation acting as an additional oxidant. Oxidation rates in high pH experiments may have been slowed by the secondary precipitation of iron oxides hindering reaction rates through grain armoring (Evangelou and Zhang, 1995). The design of our experiments and the very low extent of reaction caused by nanomolar O_2 concentrations limits these effects. For example, while trace amounts of ferric iron likely contributed to total pyrite oxidation rates in our experiments, the consumption of O_2 from solution is only sensitive to pyrite oxidation by O_2. Likewise, while small amounts of ferric oxide likely precipitated in our high pH experiments, the total amount of secondary precipitate is limited to a few micromoles based on the total moles of O_2 delivered to the system. Assuming monolayer coverage of the mineral surface, the resulting oxide layer would cover on the order of 100–1000 cm^2. Compared to the large mineral surface area present in the experiments (1–10 m^2), this mass of iron oxides is negligible. As a result, our experimental design minimizes the rate-retarding effect of grain armoring by ferric oxide at the mineral surface.

The true best estimate for the order of reaction with respect to $[H^+]$ remains a matter of debate (Smith and Shumate, 1970; McKibben and Barnes, 1986; Williamson and Rimstidt, 1994; Ciminelli and Osseo-Asare, 1995; Liu et al., 2008a). This uncertainty is likely because rate dependence of pyrite oxidation on pH acts through several mechanisms each of which could enhance or retard bulk mineral oxidation rates.

For example, electrochemical studies, such as Holmes and Crundwell (2000) and Liu et al. (2008b), demonstrated that each site of electron transfer on the pyrite surface has its own pH dependence, which additionally depends on which oxidant is acting as the electron acceptor. Holmes and Crundwell found that while the anodic site has a pH dependence of −0.5, the cathodic site has a pH dependence

of 0.14 when O_2 was the electron acceptor. However, when ferric iron was the electron acceptor, no pH dependence was observed. The "net" pH dependence then might be expected to vary with the chosen experimental parameters, such as the concentrations of dissolved O_2 or ferric iron interacting with the surface. This effect is potentially demonstrated by Holmes and Crundwell, who found a pyrite oxidation pH dependence of −0.25 to −0.5 in iron-rich leaching solutions (<21 ppm O_2) and −0.18 in oxic leaching solutions (free of ferric iron). With these observations in mind, our pH dependence of -0.25 ± 0.02 is more consistent with pyrite oxidation under low O_2 conditions. However, as we were unable to easily monitor oxidation by ferric iron in our experiments, more research is required to elucidate the nature of pH dependence in oxic and anoxic systems.

4.2. Molybdenite Oxidation Rates

4.2.1. Rate vs. $[O_2]$

To the best of our knowledge, we present the first empirically determined rate law for molybdenite oxidation at 25 °C as a function of pO_2 and pH. We find an order of reaction with respect to pO_2 of 0.5 ± 0.3, consistent with the half-order kinetics observed in our pyrite oxidation experiments. Thus, despite having a different crystal structure, molybdenite and pyrite oxidation by O_2 may share a similar rate-determining reaction mechanism. However, more experimental data at higher pO_2 are needed to reduce the high degree of uncertainty in the reaction order.

Greber et al. (2015) performed a series of aqueous and gas-phase molybdenite oxidation experiments at $<9.5 \times 10^{-6}$–1.5×10^{-3} PAL pO_2. During these experiments, the authors were able to measure increasing dissolved Mo concentrations in solution over the course of 13–14 days. However, because they did not report a mineral surface area or a rate law from their study, it is difficult to quantitatively compare their results with the rates predicted by our molybdenite oxidation experiments. Nevertheless, both studies are consistent in indicating that molybdenite oxidation can proceed at very low pO_2 values.

4.2.2. Rate vs. $[H^+]$

We were unable to discern a clear pH dependence given larger uncertainty of our molybdenite oxidation rates. Nonetheless, the data suggest that the extent of pH dependence is notably less than we observed for pyrite oxidation. One possible explanation for this difference is that molybdenite grains in solution possess significant surface charge over a wide range of pH (pH 3–11, Lu et al., 2015). Because surface charge is thought to influence the strength of mineral lattice bonds, and consequently surface reactivity, a surface charge independent of pH could lead to mineral oxidation kinetics that are independent of pH.

An electrochemical study of molybdenite oxidation could provide more insight into the pH dependence of this reaction. For instance, Cao et al. (2015) observed Mo leaching from molybdenite generally increased with increasing pH. However, they attribute increased Mo yield to increased solution concentrations of Cl oxidants at high pH, rather than increasing oxidation kinetics. Other leaching studies such as Wang et al. (2015) and Liu et al. (2017) also found that Mo yield from molybdenite leaching increased with increasing hydroxide concentrations. This observation suggests that molybdenite oxidation relies on the availability of hydroxide, and therefore the oxidation kinetics should be pH dependent. Unfortunately, neither of these studies directly addressed oxidation kinetics, which makes direct comparison of our results difficult.

4.3. Pyrite Oxidation Mechanism

Our new experimental results at low concentrations of O_2 provide valuable clues to the reaction mechanism producing a fractional-order pyrite oxidation dependence on O_2. In Fig. 6A, we systematically explore scenarios for simple surface reactions in which the kinetics in each case have a different rate-determining step. There are three elementary steps in the reaction involved in the surface-mediated reduction of an oxidant in solution. These are: (1) adsorption of oxidant A in solution to a surface site; (2) reaction of adsorbed species A to produce adsorbed species B; and (3) desorption of species B into solution, freeing a surface site for further reaction. Each of these elementary steps is reversible. For sulfide oxidation, species A is dissolved O_2, and species B includes O_2 radicals, H_2O_2, and eventually H_2O (Schoonen et al., 2006).

Previous predictions of pyrite oxidation kinetics at low O_2 have varied in part because various authors have differed in their interpretation of the reaction mechanism responsible for the fractional order kinetics. For example, Nicholson et al. (1988) proposed that pyrite oxidation was limited by O_2 adsorption to the pyrite surface, and therefore modeled the rate law using an adsorption isotherm. This rate law predicts a saturation-type behavior. At low O_2, this model predicts that pyrite oxidation would be first-order with respect to O_2, as increasing O_2 results in a simple increase in reaction rate. However, at higher O_2 the surface becomes saturated with O_2 resulting in fractional and eventually zero-order dependence on O_2 concentrations (Fig. 6B-1).

Other studies, however, have identified pyrite oxidation to be a surface-mediated process (Holmes and Crundwell, 2000; Chiriță and Schlegel, 2017). In this case, most elementary models of pyrite oxidation would either predict a first-order dependence on O_2 assuming rapid detachment of products (Fig. 6B-2), or a zero-order dependence on O_2 in the case that detachment of the products was the rate limiting step (producing an oxidation rind, Fig. 6B-3). However, these simple models fail to explain the origin of the observed half-order kinetic dependence with respect to O_2. Without a correctly identified reaction mechanism, extrapolation of the observed rates outside the range of O_2 calibrated by experiments is risky.

We can rule out reaction (3) as the rate-limiting process because it produces a zero-order reaction (Fig. 6B-3). In this case, the detachment of oxidized products is the rate-limiting step. Because the surface becomes saturated with oxidized products, changes in O_2 concentration have no further effect on the rate of dissolution. We can also rule

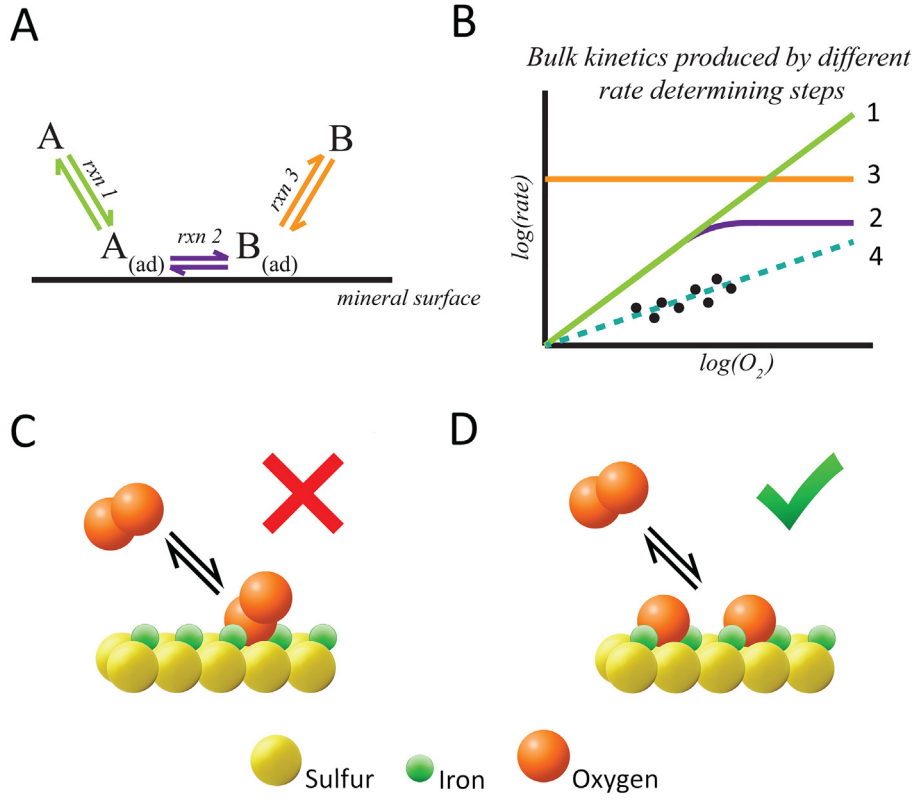

Fig. 6. (A) Schematic of the three elementary steps in a surface-catalyzed reaction. Reaction (1) is the adsorption of species A ($A_{(ad)}$ denotes the adsorbed species). Reaction (2) is the conversion of species $A_{(adsorbed)}$ to species $B_{(adsorbed)}$. Reaction (3) is the detachment of species B from the reaction surface. Each of these elementary steps is reversible. (B) Schematic showing how the rate of pyrite oxidation will vary with O_2 when limited by different elementary reactions in shown in panel A. Limitation by Reaction (1) results in a linear, first-order rate law. Limitation by Reaction (2) results in a saturation-type rate law. Limitation by Reaction (3) results in a zero-order law which is independent of O_2. Our data follow a half-order dependence with lower slope. Black points are schematic representations of the data presented in this study. (C) A simple molecular O_2 adsorption reaction would predict a first order linear dependence on O_2 at low O_2 concentrations (6B-1, 6B-2) as thus cannot explain our data. (D) Our data strongly favor a model where O_2 dissociates during adsorption to the pyrite surface, resulting in a half-order dependence on the dissolved O_2 concentration (6B-4).

out reaction (1) as the rate limiting step, since this would be expected to produce a first-order dependence of pyrite oxidation rates on the dissolved O_2 concentration—increases in dissolved O_2 directly translate to increased reaction rates.

When reaction (2) is limited by the exchange of electrons at the mineral surface, the reaction rate depends on the proportion of surface sites filled by O_2 adsorbed to the pyrite surface θ_A. In this case, the rate law takes the form:

$$r = k_2 N_T \theta_A - k_{-2} N_T \theta_B \quad (9)$$

where k_2 and k_{-2} are the forward and backward rate constants for the reversible reaction (2); N_T is the total number of reaction sites available on the mineral surface; and θ_A and θ_B are the fractions of sites occupied by $O_{2,\ ads}$ and B_{ads}, respectively (the latter of which represents the oxidized species produced by the reaction). When the reaction is far from equilibrium, the rate of the forward reaction exceeds the rate of the back reaction, so the first term in Eq. (9) dominates the rate. For the case where molecular O_2 is adsorbing to the mineral surface (Fig. 6C),θ_A takes the form of a simple adsorption isotherm:

$$\theta_A = \frac{K_A[O_2]}{1 + K_A[O_2]} \quad (10)$$

As discussed above, Nicholson et al. (1988) invoked this mechanism to explain the saturation curve response observed in their data. In the Nicholson et al (1988) model, oxidation rates are expected to be first order at low O_2 and zero order at high O_2 in accordance with Eq. (10). They hypothesized that the apparent half-order dependence was an artifact of fitting a log-linear function to the curved portion of the saturation curve. However, our new results clearly indicate that pyrite oxidation is half-order with respect to O_2, even at very low concentrations.

Instead, our new data provide strong evidence to support a mechanism where O_2 is dissociatively adsorbed to the pyrite mineral surface during reduction as shown in Fig. 6D. Previous studies have observed that after O_2 adsorbs to a mineral surface, it undergoes reduction by several electron transfers and dissociates in the process (Rosso et al., 1999; Rimstidt and Vaughan, 2003; Schoonen et al., 2006; Zhang and Anderson, 2007; Dos Santos et al., 2016).

This scenario is distinct from mono-atomic adsorption because the dissociated oxygen molecules may occupy two metal sites, which changes reaction order of surface-mediated reactions. In this case, Eq. (10) is modified:

$$\theta_A^* = \frac{(K_A[O_2])^{\frac{1}{2}}}{1 + (K_A[O_2])^{\frac{1}{2}}} \quad (11)$$

Substitution of Eq. (11) back into Eq. (9) produces a bulk oxidation rate law that is half-order with respect to O_2 over several orders of magnitude of O_2 concentration (Fig. 6B-4). Given the observed half-order dependence in our experiments, we suggest this surface-mediated mechanism explains the bulk pyrite oxidation kinetics observed in experimental studies. These results provide experimental confirmation of the dissociative chemisorption hypothesis favored by Rosso et al. (1999). Although this rate law eventually saturates at high concentrations of O_2, existing experimental data suggests that saturation requires >1 atm of pO_2. This mechanism may apply to molybdenite oxidation as well, but more data are required to more precisely define the order of reaction for molybdenite oxidation with respect to O_2.

4.4. Implications for weathering models

The new pyrite oxidation rate law presented here greatly improves our ability to constrain models of sulfide weathering at Earth's surface through time, particularly in the Archean and Proterozoic when O_2 levels are thought to have been much lower than those present today. Our data show good agreement with extrapolations of the Williamson and Rimstidt (1994) rate law, lending support to studies based on their earlier work (Reinhard et al., 2009; Reinhard et al., 2013; Johnson et al., 2014; Stüeken et al., 2012), while at the same time suggesting that the quantitative conclusions of several other studies might need to be revised to reflect more accurate kinetic models for pyrite oxidation (Bolton et al., 2006; Daines et al., 2017; Kanzaki and Kump, 2017).

For example, we observe significant change relative to the results of Daines et al. (2017) when updated with our pyrite oxidation kinetics. Daines et al. (2017) quantified the O_2 sink represented by several weathering reactions, including global sulfide oxidation as a function of pO_2, by modifying an existing reaction-transport model developed

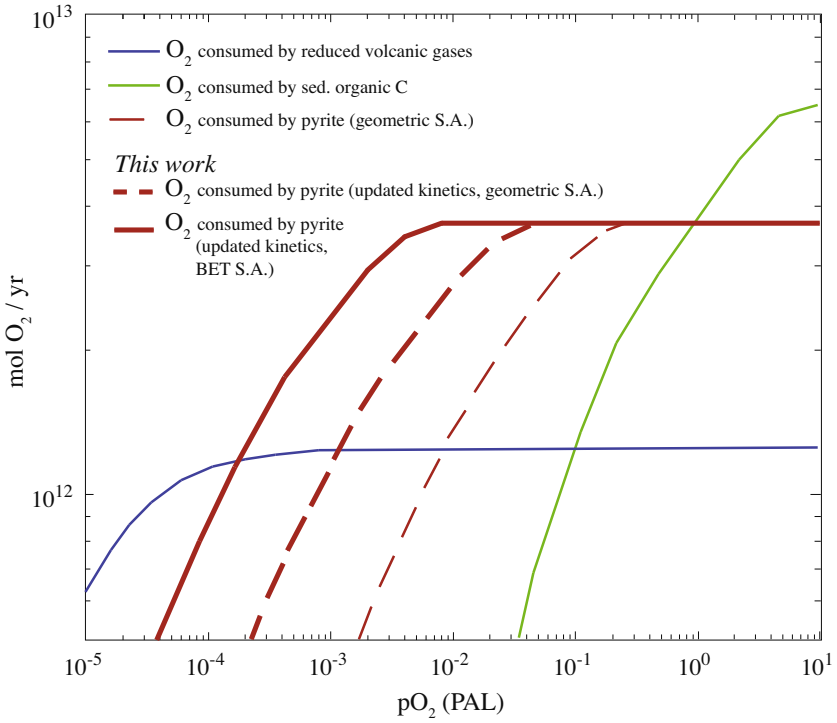

Fig. 7. Modeled global O_2 consumption as a function of pO_2 and oxidation of volcanic gasses (blue), sedimentary organic carbon (green), and sedimentary mineral sulfides (thin red dashed) (modified from Daines et al., 2017). Red bold dashed line is O_2 consumption by mineral sulfides using updated pyrite oxidation rates from this work (normalized to geometric surface areas), and red bold solid line is our final updated kinetics after correcting for the conversion from geometric to BET surface area. (For interpretation of the references to color in this figure legend, the reader is referred to the web version of this article.)

Table 3
Comparison of geometric surface areas and BET measured surface areas.

Study	Grain size (microns)	Geometric SA (m^2/g)	Initial BET SA (m^2/g)	BET/Geom. Ratio
This work	20–50	0.040	0.363	9.1
Williamson and Rimstidt (1994)	150–250	0.006	0.047	7.8
McKibben and Barnes (1986)	125–250	0.006	0.025	4.2
Moses and Herman (1991)	38–45	0.030	0.071	2.4

by Bolton et al. (2006). Importantly, the latter uses the pyrite oxidation kinetics of Smith and Shumate (1970) as a proxy for mineral sulfide oxidation rates. Using the same model framework updated with our new kinetic data we find that our new pyrite oxidation rates at low O_2 are up to an order of magnitude faster than the rate law used in these models (Fig. 5). As a result, when we recalculate the O_2 sink represented by global sulfide oxidation, we find that sulfide oxidation at low O_2 accounts for an order of magnitude greater atmospheric O_2 consumption than previously estimated (Fig. 7).

Taken at face value, these updated pyrite oxidation kinetics increase estimates of sulfate and trace metal delivery to the oceans during the Archean and Proterozoic, while potentially shifting the viable regions of atmospheric O_2 stability significantly. For example, at $pO_2 > 10^{-4}$ PAL, Fig. 7 suggests that global sulfide oxidation would act as a stronger negative feedback on increasing atmospheric O_2 than previously estimated. While this negative feedback may be offset by the reverse reaction of authigenic pyrite production in anoxic marine sediments (Daines et al., 2017), it is nonetheless a significant increase in our estimates of crustal sulfide oxidation.

Another important consideration for future sulfide weathering models is the treatment of mineral specific surface area. Weathering models commonly use geometric surface areas, which are calculated assuming spherical or cubic grains of a given diameter. However, most rate laws reported in the literature are normalized to BET measured surface areas, which are much greater than geometric surface areas. For instance, the pyrite grains used in this study initially range in diameter from 10-50 microns. If we assume an average diameter of 30 microns for cubic grains, we can calculate a geometric surface area of 0.04 m^2/g. This calculated surface area is an order of magnitude less than our pre-experiment initial BET measured surface area of 0.363 m^2/g (Table 3). It is often the case that geometric surface areas underestimate true surface area in this way, largely because imperfections on the surfaces of natural grains dramatically increase reactive surface area. Our results suggest that these different surface area normalization techniques can have a significant impact on weathering models. Studies which assume geometric grain surface area while using BET-based kinetics may significantly underestimate both the true surface area of sulfide grains and the rate of sulfide oxidation (Fig. 7).

An additional implication of our rate law for weathering models is the importance of solution pH, which is not considered fully in many published models. For instance, modern soils are highly oxygenated, and pyrite oxidation occurs mostly *in situ* due to the high abundances of O_2 and ferric iron. These reactions produce large amounts of acid, which is why acid mine drainage is such a concern for natural modern environments. Pyrite oxidation kinetics are slowest at these low pH values (compared to high-pH solutions), although they are still efficient due to the high abundance of O_2 and Fe^{3+} in modern weathering systems.

Early Earth environments with O_2 as a trace atmospheric gas, however, would be expected to behave differently. Pyrite oxidation rates would be limited by the low abundance of O_2 (Konhauser et al., 2011). Similarly, production of ferric iron would be limited. Physical weathering rates would outpace chemical weathering rates, prohibiting pyrite from oxidizing *in situ*—in contrast to what we see today (Daines et al., 2017). One possible result of these conditions is that pyrite weathering would occur largely in well-buffered riverine and floodplain/estuarine environments at potentially much higher pH values compared to those of modern soils, greatly accelerating its oxidation kinetics. Fig. 4 predicts that these elevated kinetics, even at low levels of O_2, are nearly as fast as pyrite oxidation kinetics at modern levels of O_2 and low pH solutions. While this possibility does not include the contribution by ferric iron or other oxidants, it suggests that pyrite oxidation in early Earth environments may have been much faster than previously estimated. Thus, it will be critical for future weathering models calculating sulfide oxidation as a function of pO_2 to consider the role of pH and how it varies along the transport continuum for crustal sulfides.

5. CONCLUSIONS

We present experimentally constrained pyrite and molybdenite oxidation rates and accompanying rate laws as a function of O_2 and pH at extremely low levels of O_2 (1–1000 nM O_2, equivalent to 10^{-6}–10^{-3} present atmospheric level pO_2 at equilibrium). These data were collected from mixed flow reactor experiments in buffered solutions over the course of several weeks using the highly sensitive Luminescence-Measuring Oxygen Sensor (LUMOS) to monitor consumption rates of dissolved O_2.

We extend the range of experimentally constrained pyrite oxidation rates as a function of O_2 by up to three orders of magnitude relative to previous work. We find the order of reaction to be 0.50 ± 0.04 with respect to O_2, in agreement with several previous experiments performed at higher O_2. We find an order of reaction with respect to $[H^+]$ of -0.25 ± 0.02, which is similar to, but greater than, the majority of previous studies. We also provide the first rate law for molybdenite oxidation as a function of O_2 and find it to also be half-order and kinetically similar to pyrite, although no statistically significant pH dependence was

observed. We hypothesize that this insensitivity to pH is due to the strong surface potential generated on the face of molybdenite grains, such that changing pH has little effect on the surface charge and the resulting dissolution kinetics.

Based on these results, we present a model that shows how a surface-mediated reaction mechanism can explain fractional-order kinetics with respect to O_2, consistent with previous studies that propose a surface-mediated reaction. Our new kinetic rate laws are most applicable to modeling sulfide oxidation on the early Earth under low-O_2 conditions. We encourage use of our updated kinetic data and rate laws in future efforts to model sulfide weathering under such conditions. Importantly, our rate laws identify a sensitive pH dependence that should be considered in future studies, along with a considerable increase in rate relative to some previous estimates of sulfide oxidation at low pO_2.

ACKNOWLEDGEMENTS

We are grateful for the help of Philipp Lehner and colleagues from Graz University of Technology who supplied the LUMOS oxygen sensors. The Aarhus University contribution was supported by the Poul Due Jensen Foundation. The ASU contribution was supported by FESD "Dynamics of Earth System Oxygenation" (NSF EAR 1338810 to Anbar), NASA Earth and Space Science Fellowship awarded to Johnson (18-PLANET18R-0014), and the NASA Astrobiology Institute under Cooperative Agreement No. NNA15BB03A issued through the Science Mission Directorate (to Lyons). DEC acknowledges funding from the Villum Foundation. Conversations with Lars B. Pedersen and Preben Sørensen led to the development of the mixed flow reactor approach which greatly improved this manuscript, and conversations with Shuhei Ono improved our thinking on viable reaction mechanisms and pH dependence. We thank Stuart J. Daines, Benjamin J. W. Mills, and Timothy M. Lenton for sharing the oxidative weathering model of Daines et al. (2017). The NASA astrobiology early career collaboration award to Gregory helped facilitate that aspect of the collaboration. Reviews by D. Rimstidt and other anonymous reviewers, as well as careful editorial handling by J. Farquhar greatly improved the manuscript. ACJ thanks ACE for his support.

APPENDIX A. SUPPLEMENTARY MATERIAL

Supplementary data to this article can be found online at https://doi.org/10.1016/j.gca.2019.01.022.

REFERENCES

Anbar A. D., Duan Y., Lyons T. W., Arnold G. L., Kendall B., Creaser R. A., Kaufman A. J., Gordon G. W., Scott C., Garvin J. and Buick R. (2007) A whiff of oxygen before the Great Oxidation Event? *Science* **317**, 1903–1906.

Bolton E. W., Berner R. A. and Petsch S. T. (2006) The weathering of sedimentary organic matter as a control on atmospheric O_2: II. Theoretical modeling. *Am. J. Sci.* **306**, 575–615.

Cao Z. F., Wang M. M., Zhong H., Chen N., Xia L. Y., Fan F., Liu G. Y. and Wang S. (2015) Purification of bismuthinite concentrate by selective electro-oxidation of molybdenite. *Hydrometallurgy* **154**, 95–101.

Canfield D. E., Habicht K. S. and Thamdrup B. O. (2000) The Archean sulfur cycle and the early history of atmospheric oxygen. *Science* **288**, 658–661.

Chandra A. P. and Gerson A. R. (2010) The mechanisms of pyrite oxidation and leaching: a fundamental perspective. *Surf. Sci. Rep.* **65**, 293–315.

Chiriță P. and Schlegel M. L. (2017) Pyrite oxidation in air-equilibrated solutions: an electrochemical study. *Chem. Geol.* **470**, 67–74.

Ciminelli V. S. T. and Osseo-Asare K. (1995) Kinetics of pyrite oxidation in sodium carbonate solutions. *Metall. Mater. Trans. B* **26**, 209–218.

Daines S. J., Mills B. J. W. and Lenton T. M. (2017) Atmospheric oxygen regulation at low Proterozoic levels by incomplete oxidative weathering of sedimentary organic carbon. *Nat. Commun.* **8**, 1–11.

Dos Santos E. C., de Mendonça Silva J. C. and Duarte H. A. (2016) Pyrite oxidation mechanism by oxygen in aqueous medium. *J. Phys. Chem. C* **120**, 2760–2768.

Evangelou V. P. and Zhang Y. L. (1995) A review: pyrite oxidation mechanisms and acid mine drainage prevention. *Crit. Rev. Environ. Sci. Technol.* **25**, 141–199.

Garcia-Robledo E., Padilla C. C., Aldunate M., Stewart F. J., Ulloa O., Paulmier A., Gregori G. and Revsbech N. P. (2017) Cryptic oxygen cycling in anoxic marine zones. *Proc. Natl. Acad. Sci.* **114**, 8319–8324.

Gartman A. and Luther G. W. (2014) Oxidation of synthesized sub-micron pyrite (FeS_2) in seawater. *Geochim. Cosmochim. Acta* **144**, 96–108.

Greaney A. T., Rudnick R. L. and Gaschnig R. M. (2016) Crustal sources of Molybdenum. *Goldschmidt Conference, Yokohama Japan*.

Greber N. D., Mäder U. and Nägler T. F. (2015) Experimental dissolution of molybdenum-sulphides at low oxygen concentrations: a first-order approximation of late Archean atmospheric conditions. *Earth Space Sci.* **2**, 173–180.

Gregory D. D., Lyons T. W., Large R. R., Jiang G., Stepanov A. S., Diamond C. W., Figueroa M. C. and Olin P. (2017) Whole rock and discrete pyrite geochemistry as complementary tracers of ancient ocean chemistry: an example from the Neoproterozoic Doushantuo Formation, China. *Geochim. Cosmochim. Acta* **216**, 201–220.

Holmes P. R. and Crundwell F. K. (2000) The kinetics of the oxidation of pyrite by ferric ions and dissolved oxygen: an electrochemical study. *Geochim. Cosmochim. Acta* **64**, 263–274.

Johnson J. E., Gerpheide A., Lamb M. P. and Fischer W. W. (2014) O_2 constraints from Paleoproterozoic detrital pyrite and uraninite. *Bulletin* **126**, 813–830.

Kanzaki Y. and Kump L. R. (2017) Biotic effects on oxygen consumption during weathering: implications for the second rise of oxygen. *Geology* **45**, 611–614.

Kendall B., Creaser R. A., Reinhard C. T., Lyons T. W. and Anbar A. D. (2015) Transient episodes of mild environmental oxygenation and oxidative continental weathering during the late Archean. *Sci. Adv.* **1**, 1–6.

Konhauser K. O., Lalonde S. V., Planavsky N. J., Pecoits E., Lyons T. W., Mojzsis S. J., Rouxel O. J., Barley M. E., Rosyere C., Fralick P. W., Kump L. R. and Bekker A. (2011) Aerobic bacterial pyrite oxidation and acid rock drainage during the Great Oxidation Event. *Nature* **478**, 369–374.

Lehner P., Larndorfer C., Garcia-Robledo E., Larsen M., Borisov S. M., Revsbech N. P., Glud R. N., Canfield D. E. and Klimant I. (2015) LUMOS-A sensitive and reliable optode system for measuring dissolved oxygen in the nanomolar range. *PLoS ONE* **10**, e0128125.

Liu R., Wolfe A. L., Dzombak D. A., Stewart B. W. and Capo R. C. (2008a) Comparison of dissolution under oxic acid drainage conditions for eight sedimentary and hydrothermal pyrite samples. *Environ. Geol.* **56**, 171–182.

Liu R., Wolfe A. L., Dzombak D. A., Horwitz C. P., Stewart B. W. and Capo R. C. (2008b) Electrochemical study of hydrothermal and sedimentary pyrite dissolution. *Appl. Geochem.* **23**, 2724–2734.

Liu Z. X., Sun L., Hu J., Wu X. W., Xiao Y., Xiang Y. H., He Z. J. and lan Yin Z. (2017) Selective extraction of molybdenum from copper concentrate by air oxidation in alkaline solution. *Hydrometallurgy* **169**, 9–15.

Lu Z., Liu Q., Xu Z. and Zeng H. (2015) Probing anisotropic surface properties of molybdenite by direct force measurements. *Langmuir* **31**, 11409–11418.

McKibben M. A. (1984) *Kinetics of Aqueous Oxidation of Pyrite by Ferric Iron, Oxygen and Hydrogen Peroxide from pH l-4 and 20-4°C: Ph.D. Dissertation*. Penn. State Univ., p. 160.

McKibben M. A. and Barnes H. L. (1986) Oxidation of pyrite in low temperature acidic solutions: rate laws and surface textures. *Geochim. Cosmochim. Acta* **50**, 1509–1520.

Moses C. O. and Herman J. S. (1991) Pyrite oxidation at circumneutral pH. *Geochim. Cosmochim. Acta* **55**, 471–482.

Nicholson R. V., Gillham R. W. and Reardon E. J. (1988) Pyrite oxidation in carbonate-buffered solution: 1. Experimental kinetics. *Geochimica et Cosmochimica Acta* **52**, 1077–1085.

Paschka M. G. (2001) *Kinetics of Pyrite Oxidation. M.S. Thesis*. Carnegie Mellon University, Civil and Environmental Engineering, Pittsburgh, PA.

Reinhard C. T., Raiswell R., Scott C., Anbar A. D. and Lyons T. W. (2009) A late Archean sulfidic sea stimulated by early oxidative weathering of the continents. *Science* **326**, 713–716.

Reinhard C. T., Lalonde S. V. and Lyons T. W. (2013) Oxidative sulfide dissolution on the early Earth. *Chem. Geol.* **362**, 44–55.

Rimstidt J. D. and Vaughan D. J. (2003) Pyrite oxidation: a state-of-the-art assessment of the reaction mechanism. *Geochim. Cosmochim. Acta* **67**, 873–880.

Rosso K. M., Becker U. and Hochella M. F. (1999) The interaction of pyrite 100 surfaces with O2 and H2O: fundamental oxidation mechanisms. *Am. Mineral.* **84**, 1549–1561.

Sander R. (2015) Compilation of Henry's law constants (version 4.0) for water as solvent. *Atmos. Chem. Phys.* **15**, 4399–4981. https://doi.org/10.5194/acp-15-4399-2015.

Schoonen M. A., Cohn C. A., Roemer E., Laffers R., Simon S. R. and O'Riordan T. (2006) Mineral-induced formation of reactive oxygen species. *Rev. Mineral. Geochem.* **64**, 179–221.

Scott C., Lyons T. W., Bekker A., Shen Y., Poulton S. W., Chu X. and Anbar A. D. (2008) Tracing the stepwise oxygenation of the Proterozoic ocean. *Nature* **452**, 456–459.

Smith E. E. and Shumate K. (1970) *Sulfide to Sulfate Reaction Mechanism: A Study of the Sulfide to Sulfate Reaction Mechanism as it Relates to the Formation of Acid Mine Waters*. U.S. Federal Water Quality Administration, pp. 1–115.

Stüeken E. E., Catling D. C. and Buick R. (2012) Contributions to late Archaean sulphur cycling by life on land. *Nat. Geosci.* **5**, 722.

Wang M., Wei C., Fan G., Li M., Deng Z. and Wang S. (2015) Selective extraction of Mo from a Ni-Mo ore using pressure alkaline leaching. *Hydrometallurgy* **153**, 6–11. Available at: http://dx.doi.org/10.1016/j.hydromet.2015.01.008.

Williamson M. A. and Rimstidt J. D. (1994) The kinetics and electrochemical rate-determining step of aqueous pyrite oxidation. *Geochim. Cosmochim. Acta* **58**, 5443–5454.

Zhang T. and Anderson A. B. (2007) Oxygen reduction on platinum electrodes in base: theoretical study. *Electrochim. Acta* **53**, 982–989.

Associate editor: James Farquhar